Stereo-SCIDAR: optical turbulence profiling with high sensitivity using a modified SCIDAR instrument

H. W. Shepherd,[1] J. Osborn,[1]* R. W. Wilson,[1] T. Butterley,[1] R. Avila,[2] V. S. Dhillon[3] and T. J. Morris[1]

[1]*Department of Physics, Centre for Advanced Instrumentation, University of Durham, South Road, Durham DH1 3LE, UK*
[2]*Centro de Fisica Aplicada y Technolgìa Avanzada, Universidad Nacional Autònoma de Mèxico, A.P. 1-1010, Santiago de Querètaro, Querètaro 76000, Mexico*
[3]*Department of Physics and Astronomy, University of Sheffield, Sheffield S3 7RH, UK*

ABSTRACT
The next generation of adaptive optics systems will require tomographic reconstruction techniques to map the optical refractive index fluctuations, generated by the atmospheric turbulence, along the line of sight to the astronomical target. These systems can be enhanced with data from an external atmospheric profiler. This is important for Extremely Large Telescope scale tomography. Here we propose a new instrument which utilizes the generalized Scintillation Detection And Ranging (SCIDAR) technique to allow high sensitivity vertical profiles of the atmospheric optical turbulence and wind velocity profile above astronomical observatories. The new approach, which we refer to as 'stereo-SCIDAR', uses a stereoscopic system with the scintillation pattern from each star of a double-star target incident on a separate detector. Separating the pupil images for each star has several advantages including increased magnitude difference tolerance for the target stars; negating the need for re-calibration due to the normalization errors usually associated with SCIDAR; an increase of at least a factor of 2 in the signal-to-noise ratio of the cross-covariance function and hence the profile for equal magnitude target stars and up to a factor of 16 improvement for targets of 3 mag difference and easier real-time reconstruction of the wind-velocity profile. Theoretical response functions are calculated for the instrument, and the performance is investigated using a Monte Carlo simulation. The technique is demonstrated using data recorded at the 2.5-m Nordic Optical Telescope and the 1.0-m Jacobus Kapteyn Telescope, both on La Palma.

Key words: atmospheric effects – instrumentation: adaptive optics – site testing.

1 INTRODUCTION AND THEORY

Several techniques have been implemented to estimate the atmospheric turbulence profile, measured as the refractive index structure constant, $C_n^2(h)$, and wind velocity, both as a function of altitude. The most widely exploited are Multi Aperture Scintillation System (MASS; Tokovinin & Kornilov 2007), Scintillation Detection And Ranging (SCIDAR; Vernin & Roddier 1973) and Slope Detection And Ranging (SLODAR; Wilson 2002). MASS is not intended as a high vertical-resolution technique. It has a limited logarithmic vertical resolution and the high altitude response is very broad (Tokovinin & Kornilov 2007). Here, we only address high altitude-resolution techniques and therefore we will only discuss

SLODAR and SCIDAR. Both SLODAR and SCIDAR are triangulation techniques in which the atmospheric turbulence profile is recovered from either the correlation of wavefront slopes in the case of SLODAR, or scintillation intensity patterns in the case of SCIDAR, for two target stars with a known angular separation. A simplified schematic is shown in Fig. 1.

For the next generation of Extremely Large Telescopes (ELT) the knowledge of the turbulence profile will become essential to the efficient running of the observatory and adaptive optics (AO) systems. Tomographic AO systems combine information from several off-axis wavefront sensors to estimate the optical phase aberrations in the volume of turbulence in a given target direction or field of regard. These multiwavefront sensor systems can build an atmospheric profile using the internal wavefront sensor data using the SLODAR method (Cortés et al. 2012). External profilers can provide information which is always of the highest altitude
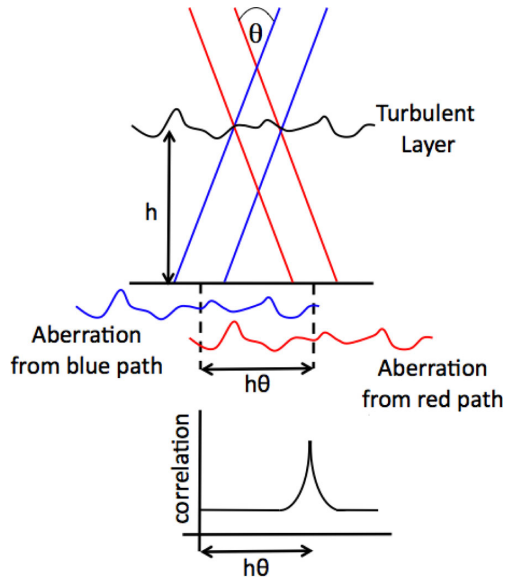
*E-mail: james.osborn@durham.ac.uk

Figure 1. If a turbulent layer at height, h, is illuminated by two stars of angular separation, θ, then two copies of the aberration will be made on the ground separated by a distance $h\theta$. By cross-correlating either the centroid positions from a Shack–Hartmann wavefront sensor (SLODAR) or the intensity patterns (SCIDAR) we can triangulate the height of the turbulent layer and the amplitude of the correlation peak corresponds to the strength of the layer.

resolution irrespective of the ELT AO wavefront sensor configuration and is independent of the AO system.

Externally generated profiles can be used to augment information derived from internal WFS data and assist observatory operations. These tasks could include validation of the performance of the AO instrumentation; comparison of performance with calculated error budgets; diagnosis of system performance issues at an early stage; collection of site statistics; validation and feedback into meteorological forecasting models (Masciadri & Lascaux 2012); pre-optimization of AO control matrices to minimize telescope down-time between observations; construction of AO control matrices for fields without any bright targets and potentially the scheduling of AO observations. However, the precise role of external profilers in the ELT era is still an area of active research and is outside the intended scope of this paper.

Turbulence profilers such as SLODAR or SCIDAR can also supply wind velocity measurements which will allow the tomographic reconstructors to use temporal information in the reconstruction process. Several smart reconstructors (e.g. linear quadratic control; Folcher & Carbillet 2011) require real-time wind velocity profiles to optimize the AO control algorithms. The combined atmospheric turbulence strength and velocity profile can be used to calculate atmospheric parameters important for the real-time optimization of AO systems, such as the isoplanatic angle and coherence time.

In this paper we discuss the SCIDAR technique. SCIDAR has the capability to determine the atmospheric profile to a higher resolution than SLODAR because the autocovariance function of the scintillation pattern from a single turbulent layer is narrower than that of the wavefront slopes, i.e. the spatial scale of the scintillation is smaller than the minimum wavefront sensor sampling of the phase, allowing for higher altitude resolution profiling. SCIDAR was originally proposed by Vernin & Roddier (1973), in which the turbulence profile is determined by processing short exposure images of the scintillation

pattern observed from a double star. SCIDAR is limited in that it is insensitive to turbulence at the ground, due to lack of propagation distance required to develop scintillation. Fuchs, Tallon & Vernin (1994) introduced generalized-SCIDAR with the suggestion that the analysis plane did not necessarily need to be at the telescope pupil. A conjugate position larger than 1 km below the pupil was suggested by Fuchs, Tallon & Vernin (1998) and even larger distances were used in the first implementation of generalized-SCIDAR by Avila, Vernin & Masciadri (1997). This extends the propagation distance of the light path and therefore allows the phase aberrations induced by the surface turbulent layer to develop into intensity fluctuations, which can be measured.

The theoretical resolution for SCIDAR is defined by the Fresnel zone size for a given altitude of the turbulent layer and is given by (Prieur, Daigne & Avila 2001)

$$\delta h(z) = 0.78 \frac{\sqrt{\lambda z}}{\theta}, \tag{1}$$

where z is the propagation distance to the layer and is given by $z = |h - h_{\rm conj}|$, where $h_{\rm conj}$ is the conjugate altitude of the detector, or analysis plane, and h is the altitude of the turbulent, λ is the wavelength and θ is the angular separation of the target stars. Throughout this paper the analysis assumes a zenith angle, $\theta_z = 0$. To generalize to other zenith angles, one would replace z by $z \sec \theta_z$. The altitude resolution for SCIDAR is a function of the propagation distance and target star separation. For larger propagation distances the spatial scale of the intensity speckle patterns is larger, reducing the altitude resolution. Stars with a wider separation will increase the altitude resolution but also reduce the maximum profiling altitude, as we can only recover the profile up to an altitude where the projected pupils from the two stars overlap. The maximum altitude that we can observe a layer is therefore,

$$h_{\rm max} = \frac{D}{\theta}, \tag{2}$$

where D is the diameter of the telescope pupil. The maximum altitude will actually be lower than this in the case where the analysis plane is positioned away from the telescope pupil. In this case diffraction through the pupil will distort the intensity distribution at the edge of the pupil (outer, secondary and spiders) and will need to be blocked. This will effectively reduce the diameter of the telescope. The width of the primary diffraction ring is independent of telescope size and is given by the Fresnel radius, $r_{\rm F} = \sqrt{\lambda h_{\rm conj}}$. This ring is substantially larger than the others and so only this outer one is blocked in order to retain a large fraction of the telescope size (Osborn et al. 2011). Equation (2) is modified to

$$h_{\rm max} = \frac{(D - r_{\rm F})}{\theta}. \tag{3}$$

For a given telescope, θ should be selected so that $h_{\rm max}$ is approximately 20 km, the maximum expected altitude of the tropopause and hence the maximum altitude for any optical turbulence.

To improve the sensitivity, efficiency and resolution of generalized-SCIDAR we have designed and built a new instrument with two cameras, one for each target star, named stereo-SCIDAR. Separating the intensity patterns from each star on to two independent cameras increases the signal-to-noise ratio of the profile, allows a greater magnitude difference of the targets and circumvents known normalization issues with conventional single camera generalized-SCIDAR data reduction (Avila & Cuevas 2009).

Section 2 describes the stereo-SCIDAR technique including the optomechanical design, the theoretical derivation of the response
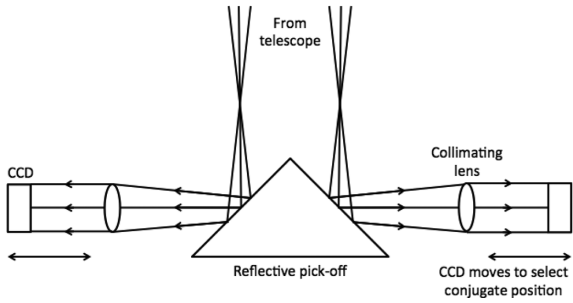
Figure 2. A schematic layout of the stereo-SCIDAR instrument. The reflecting pick off in the centre directs the light from each star to one arm of the instrument. The light in each arm is then collimated, and the resulting intensity pattern is imaged on to the CCD detector. Each CCD detector is attached to a linear stage which controls the altitude of the analysis plane imaged by the detector.

functions and an overview of the associated advantages. Section 3 explains the data reduction algorithm and the profile fitting. Section 4 presents a selection of on-sky results. We conclude in section 5.

2 STEREO-SCIDAR

2.1 Optomechanical design

Conventionally, SCIDAR is implemented with a single camera, which records the overlapping pupil images. Stereo-SCIDAR utilizes a separate camera for each pupil image. The prototype stereo-SCIDAR instrument has been deployed on the 2.5-m Nordic Optical Telescope (NOT) during 2013 March and the 1-m Jacobus Kapteyn Telescope (JKT) in 2013 May, July and September. The instrument uses a reflective glass wedge to separate the beams from each of the two stars on to two separate CCD detectors. One of the images is inverted in software to ensure that both images have the same on-sky orientation. A sketch of the instrumental design is shown in Fig. 2. In this implementation two Andor Luca S EMCCD detectors were used. The cameras have a maximum frame rate of ∼90 Hz and we use an exposure time of 2 ms. The NOT has an aperture diameter of 2.5 m and an effective focal length of 28.2 m. A collimating lens of focal length 32 mm leads to a beam diameter of 2.8 mm.

A two camera system can emulate any functionality of a single camera system by simply adding together the two images. However, there are several advantages to the two camera system at the cost of a more complicated optomechanical and electronic design.

2.2 Cross-covariance functions

Using two cameras instead of one changes the profile restoration process for SCIDAR. When using a single camera, the pupil images from each target star overlap on the CCD, with an offset depending on the conjugate altitude of the analysis plane and on the angular separation of the targets (at the telescope pupil the two images will be completely superimposed). One calculates the autocovariance function of the image which is normalized by the autocovariance of the mean image. Each turbulent layer will contribute three peaks to the autocovariance function, as the intensity pattern from each star correlates with the intensity pattern with the other star and with itself (Fig. 3, right). The profile can be restored by fitting the 1D cut of the covariance peaks in the direction between the two stars with the theoretical response functions of the instrument. The response
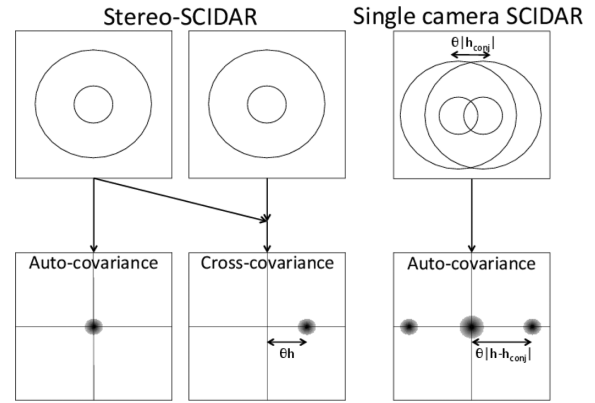

Figure 3. The cross-covariance function for the two stereo-SCIDAR frames results in a single peak offset by θh (left). The autocovariance function of single camera SCIDAR results in three peaks for each layer. One at the centre of the autocovariance and one at plus and minus $\theta|h - h_{conj}|$ (right).
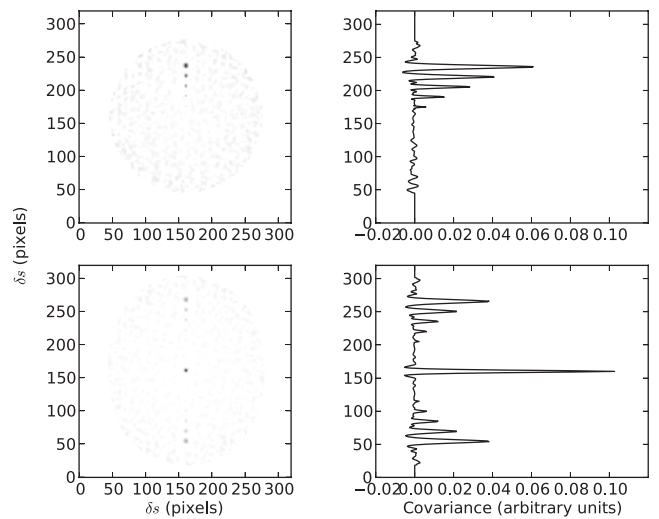

Figure 4. 2D covariance plots for stereo-SCIDAR (upper) and single camera generalized-SCIDAR (lower) for an atmospheric simulation containing six equal strength turbulent layers at 2 km spacing between 0 and 10 km, inclusive. A vertical cut through each covariance function is shown on the right. δs is the position in the covariance function. We see that for single camera SCIDAR we have two sets of spatially separated peaks and one set of overlapping peaks at the centre. For stereo-SCIDAR we only have one set. Both plots have the same grey-scale, the correlation peaks for stereo-SCIDAR are larger in magnitude than that of single camera generalized-SCIDAR.

functions map the atmospheric optical turbulence profile on to the covariance function (i.e. what the instrument actually measures).

For a two camera system we normalize each pupil image to have the same mean intensity and then calculate the cross-covariance of the two individual intensity patterns. This cross-covariance can be normalized by the cross-covariance of the mean pupil images. In this way the stereo-SCIDAR cross-covariance function only has one set of correlation peaks from the centre outwards in the direction parallel to the position angle of the two binary target stars (Fig. 3, left). Fig. 4 shows example simulated covariance functions for stereo-SCIDAR and for single camera SCIDAR.

The spatiotemporal covariance (cross or auto) can be computed by calculating the covariance function with increasing offsets in the frame number. If we correlate one frame with itself, this gives us the d$t = 0$ plane. The correlation of one frame with the subsequent

frame would be the $dt = 1$ plane and with the preceding frame would be the $dt = -1$ plane in the spatiotemporal covariance.

2.3 Theoretical background

2.3.1 Kolmogorov turbulence

The propagation of starlight through a turbulent layer in the atmosphere leads to an intensity distribution at the telescope aperture. If we assume that the turbulence has a Kolmogorov power spectrum then the spatial intensity power spectrum at the ground is given by

$$\Phi_I(f) = 3.9 \times 10^{-2} k^2 f^{-11/3} \int_0^\infty C_n^2(z) \sin^2(\pi \lambda z f^2) \, dh, \qquad (4)$$

where k is the wavenumber of the light from the star, and f the spatial frequency of the atmospheric turbulence (Roddier 1981). For Kolmogorov turbulence this is valid over the inertial range $1/L_0 \le f \le 1/l_0$, where L_0 and l_0 are the outer and inner scales of the turbulence, respectively.

The above equation forms the basis of the SCIDAR response functions. It should be noted that it is only valid for weak-scintillation conditions and in the monochromatic light approximation. In SCIDAR techniques, scintillation only occasionally fails to be weak. In such cases, the power spectrum of the actual scintillation has lower maximum values and presents a noisy aspect, as shown by Tokovinin & Kornilov (2007) from numerical simulations. Essentially, in the strong fluctuation regime, the effect of each independent turbulent layer can no longer be assumed to be additive.

The validity of the monochromatic approximation has been well justified for SCIDAR-like techniques (Tokovinin 2003). Here we use polychromatic light, only filtered by the wavelength-dependent quantum efficiency of our camera. All SCIDAR systems use polychromatic light, in order to collect sufficient photons for the analysis. We have developed a Monte Carlo simulation to compare the monochromatic covariance function with a polychromatic one. The simulation included a test atmosphere containing six layers separated by 2 km and all having equal turbulence strength, this was to confirm that the effect of several turbulent layers was additive (weak fluctuation regime), as is assumed by SCIDAR. The polychromatic pupil images were generated by summing together six images generated with wavelengths between 500 and 800 nm, outside of this range the quantum efficiency of the cameras ensure that the throughput is negligible. The images were weighted by the wavelength-dependent quantum efficiency of the camera and the stellar spectral emission. The transmission spectrum of the atmosphere in the visible was assumed to be uniform. The wavelength weights are as shown in Table 1.

We compared the simulated polychromatic covariance functions with the monochromatic case (at $\lambda = 500$ nm). The simulation showed negligible difference between the two covariance functions

Table 1. Wavelength weights for polychromatic simulation.

Wavelength (nm)	Andor Luca QE per cent	Stellar flux/maximum	Weight
500	0.52	1.00	0.21
550	0.5	0.92	0.19
600	0.49	0.86	0.17
650	0.45	0.78	0.15
700	0.38	0.77	0.12
750	0.29	0.75	0.09
800	0.22	0.73	0.07

meaning that it is indeed appropriate to use the monochromatic equations to generate the response functions of SCIDAR.

2.3.2 SCIDAR response functions

The response function is the response of the instrument to a thin layer at a given altitude and maps the output of the instrument (i.e. the covariance function) to the actual turbulence profile. The stereo-SCIDAR response functions are identical to those of conventional SCIDAR, the difference between the techniques is in how the covariance function is generated and normalized.

The quantity measured by the stereo-SCIDAR instrument is the normalized scintillation spatial autocovariance function $B(\mathbf{r})$:

$$B(\mathbf{r}) = \frac{\langle [I_1(\mathbf{x}) - \langle I_1 \rangle][I_2(\mathbf{x} + \mathbf{r}) - \langle I_2 \rangle] \rangle}{\langle I_1 \rangle \langle I_2 \rangle}, \qquad (5)$$

where $I_n(\mathbf{x})$ is the normalized intensity distribution in the analysis plane for a single star, n. The angled brackets denote an ensemble average.

As the power spectrum of the intensity variations for both stars is identical, the autocovariance of the intensity patterns can be related to the power spectrum of the scintillation using the Wiener–Khintchine theorem. This states that the autocovariance corresponds to the Fourier transform of the power spectrum. As the power spectrum is rotationally symmetric, this can be taken to be a Hankel transform (Roddier 1981):

$$B(\mathbf{r}) = 2\pi \int_0^\infty f \Phi_I(f) J_0(2\pi r f) \, df, \qquad (6)$$

where J_0 is a Bessel function of the first kind. By combining equations (4) and (6), a single turbulent layer at propagation distance z will give

$$B(\mathbf{r}, z) = 3.9 \times 10^{-2} 2\pi k^2 C_n^2(z) \, dh$$

$$\times \int_0^\infty f^{-8/3} \sin^2(\pi \lambda z f^2) J_0(2\pi r f) \, df. \qquad (7)$$

This is the intensity fluctuation autocovariance density per unit altitude produced by a layer located at a distance z. We also define a further quantity $B'(\mathbf{r}, z)$, corresponding to $B(\mathbf{r}, z)$ for unit turbulence strength (i.e. $B(\mathbf{r}, z)/C_n^2(h) \, dh$). We define this quantity to be the stereo-SCIDAR response function for unit turbulence at altitude z.

The measured star autocovariance ($B(\mathbf{r}, \theta)$) corresponds to

$$B(\mathbf{r}, z) = \int C_n^2(z) B'(\mathbf{r}, z) \, dz. \qquad (8)$$

Example SCIDAR response functions are shown in Fig. 5 for five propagation distances. As the propagation distance increases, the cross-covariance signal increases, but also becomes wider, decreasing the altitude resolution.

2.3.3 Single camera SCIDAR autocovariance functions

In single camera SCIDAR the measured autocovariance function can be written as (Tokovinin 1997)

$$B(\mathbf{r}, \boldsymbol{\theta}) = \int A_1 B(\mathbf{r}) + A_2 (B(\mathbf{r} - \boldsymbol{\theta} z, z) + B(\mathbf{r} + \boldsymbol{\theta} z, z)) \, dz, \qquad (9)$$

where

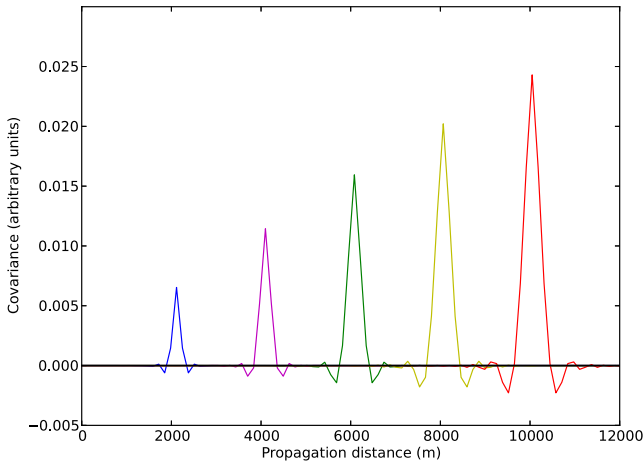$$A_1 = \frac{1 + \gamma^2}{(1 + \gamma)^2}, \qquad (10)$$

Figure 5. A subsample of SCIDAR response functions corresponding to five propagation distances equally spaced between 2 and 10 km. Here we plot the propagation distance and not absolute altitude and so, for example, the result is identical for a layer at 2 km whilst conjugate to 0 km and for a layer at 0 km whilst conjugate to −2 km.

$$A_2 = \frac{\gamma}{(1 + \gamma)^2} \qquad (11)$$

and

$$\gamma = 10^{-0.4\Delta m}, \qquad (12)$$

where Δm is the relative magnitude difference of the target stars and $B(r)$ is the scintillation autocovariance function. Each term within the integral of equation (9) corresponds to a set of peaks in the autocovariance function (Fig. 4). To recover the turbulence profile we take either of the lateral sets of peaks from the triplet $(B(r - \theta|h - h_{conj}|)$ or $B(r + \theta|h - h_{conj}|))$ leading away from the centre and fit them to the response functions of the instrument. From equation (9) we see that the amplitude of these peaks, and hence the visibility, is multiplied by A_2. It can be shown that the uncertainty in the optical turbulence profile $\propto A_1/A_2$ (Prieur et al. 2001). Therefore, for larger magnitude differences the visibility of the correlation peaks is reduced, hence reducing the signal-to-noise ratio. If both stars have the same brightness, then $A_1 = 0.5$ and $A_2 = 0.25$. However, if there is a 2 mag difference in brightness, then $\gamma = 0.16$, $A_1 = 0.76$ and $A_2 = 0.12$.

2.4 Advantages of stereo-SCIDAR

2.4.1 Normalization

In conventional single camera generalized-SCIDAR the pupil patterns from the two target stars overlap. This overlap results in a lack of contrast in the combined pupil image and hence a loss of information. The loss of contrast means that the peaks in the covariance function that are used to recover the profile are reduced in amplitude.

If the analysis plane is conjugate to the ground, then the pupil images are entirely overlapping and it can be shown that the amplitude of the lateral peaks is proportional to A_2. When the pupils are fully superimposed the covariance is underestimated by a factor of 4. As the analysis plane is moved away from the ground the images separate on the detector leading to a more complicated, height-dependent contrast adjustment. This has been addressed in detail by Avila & Cuevas (2009). They show that using the autocovariance

of the average overlapping pupil images to normalize the individual autocovariance can actually introduce an error of the order of 10 s of per cent depending on the telescope aperture geometry and the altitude of the layers. This is now understood and can be corrected using theoretical approximations. However, this issue can be entirely avoided by separating the pupil images in stereo-SCIDAR.

It is worth noting that the normalization error only applies when the defocussed pupil images are superimposed, which is the case for most generalized-SCIDAR systems in use. Low-layer SCIDAR (LOLAS; Avila et al. (2008) is a variation of the SCIDAR method in which the pupils are also entirely separated, but still on one detector, and so also negates the aforementioned issue. High vertical-resolution generalized-SCIDAR (Masciadri et al. 2010) also by-passes this normalization issue by re-distributing the measured turbulence strength into discrete altitudes defined in the spatiotemporal autocovariance.

2.4.2 Improved target magnitude difference range

The stellar magnitude difference for the targets for generalized-SCIDAR when the defocussed images are superimposed is limited to ∼2.5 mag (García-Lorenzo & Fuensalida 2011) at most and often only 1 mag (Masciadri et al. 2010).

The equivalent A_2 value for stereo-SCIDAR is 1.0 (Section 2.3.1, equation 8) and is independent of magnitude difference, Δm, of the target stars. Stereo-SCIDAR is limited only by signal. This means that the signal-to-noise ratio is independent of the magnitude difference. Therefore, larger stellar magnitude differences can be tolerated and hence a greater number of targets are available. This is particularly important on smaller telescopes. For example on the JKT (1 m, La Palma), using single camera SCIDAR we have a gap in the right accession (RA) angle of 5 h in which there are no suitable targets ($\Delta m < 1.5$). Using stereo-SCIDAR we have valid targets for all RA angles.

Fig. 6 shows the 1D cut of simulated cross-covariance functions for stereo-SCIDAR and for conventional generalized-SCIDAR. The simulation was for a 2.5-m telescope, 30 arcsec target separation,
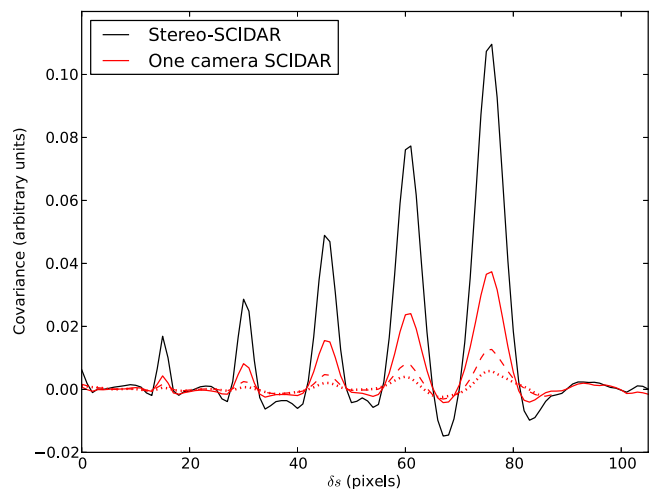

Figure 6. 1D cut of simulated covariance functions for stereo-SCIDAR and single camera SCIDAR. The solid lines are for the case where the two target stars have the same magnitude, dashed lines indicate a 2 mag difference ($m_1 = 4$, $m_2 = 6$) and the dotted lines indicate a 3 mag difference in brightness ($m_1 = 4$, $m_2 = 7$). Note that for the stereo-SCIDAR case the three lines are co-incident. There is no loss of contrast for increasing magnitude difference.

−3000 m conjugate altitude and 1$^{\rm m}$ of data. We show the covariance function for equal magnitude stars and for targets with 2 and 3 mag difference in brightness. The generalized-SCIDAR covariance peaks becomes smaller and hence increasingly more noisy for larger magnitude differences, due to contrast reduction explained in Section 2.3.3. The reduction in amplitude can be tolerated and included in the theoretical correction described above, however, the lower signal-to-noise ratio is a fundamental problem and limits the possible magnitude difference of the targets for single camera generalized-SCIDAR.

2.4.3 Sensitivity

The sensitivity of the SCIDAR method is well documented in the literature (Tokovinin 1997; Prieur et al. 2001, 2004). The approach taken is to calculate the sensitivity at a position j in the covariance function, corresponding to a layer at altitude h_j, in the presence of an assumed turbulent atmosphere with a dominant layer at altitude H_0.

The statistical rms noise of $B(\boldsymbol{r})$ for a single frame can be approximated by dividing the sum of the independent noise variances (scintillation, readout and shot noise in this case, but others can be included) by the square root of the number of speckles in the overlapping area of projected pupils at altitude h_j. The number of speckles in the area of overlap is equal to the area of overlap of the projected pupils divided by the area of the dominant speckle size,

$$A_{\rm F} = \frac{f(r/D)\pi(D/2)^2}{\pi r_{\rm F}^2},\tag{13}$$

where $f(x) = \arccos(x) - x(1 - x^2)^{1/2}$ is the fraction of overlapping area of two full discs separated by a distance x in diameter units, where $x = r/D$ and $r_{\rm F} = \sqrt{\lambda H_0}/2$ is the Fresnel zone radius of the most significant speckle scale, i.e. the speckle with the largest σ_I^2, from a layer at altitude H_0 (Tokovinin 1997). Therefore,

$$\Delta B(r) = \frac{(A_1 B(0) + (R/N_\gamma)^2 + 1/N_\gamma)}{\sqrt{\frac{D^2 f(r)}{\lambda H_0}}},\tag{14}$$

where $A_1 B(0)$ is the scintillation variance, σ_I^2, and is equal to the amplitude of the central peak in the autocovariance function, R is the rms readout noise per scintillation speckle and N_γ is the number of photons received during the exposure per scintillation speckle.

This can be converted into the sensitivity in the turbulence profile by dividing by the scintillation variance of a layer with unit strength at altitude h_j ($\sigma_{I,j}^2 = 19.12\lambda^{-7/6}h_j^{5/6}$), using

$$\Delta\tilde{J}_j = \frac{5.23\times10^{-2}\lambda^{5/3}h_j^{-5/6}H_0^{1/2}(A_1 B(0) + (R/N_\gamma)^2 + 1/N_\gamma)}{A_2 D\sqrt{f(x)T/\tau_{\rm c}}},\tag{15}$$

where $J = \int_{h_1}^{h_2} C_n^2(h)\,{\rm d}h$ is the integrated turbulence strength over some altitude range and has units $m^{1/3}$. To calculate the rms noise of the profile, $\Delta\tilde{J}_j$, at position j, for the recovered profile we must include the number of independent realizations used to generate the profile. This can be approximated by $T/\tau_{\rm c}$, where T is the integration time and $\tau_{\rm c}$ the frame rate.

The above equations are valid for completely overlapping pupils, i.e. $h_{\rm conj} = 0$, for targets of equal magnitude $A_1 = 0.5$ and $A_2 = 0.25$. In the extreme of fully separated pupils, as with stereo-SCIDAR and LOLAS, $A_1 = A_2 = 1$. As the sensitivity of SCIDAR is proportional to A_1/A_2, stereo-SCIDAR can achieve double the sensitivity.
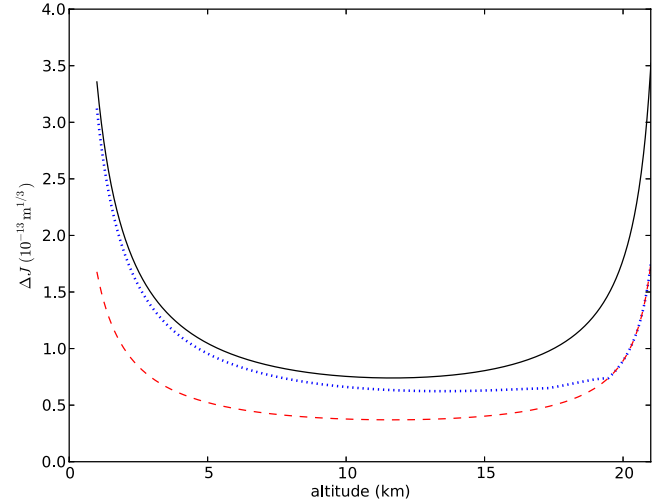

Figure 7. RMS noise of the turbulence profile, ΔJ, as a function of layer altitude for a single independent frame. The telescope diameter is 1 m and $\theta = 10''$. The solid line shows the completely overlapping pupil case. The dashed line is the completely separated case, with a factor of 2 reduction in the noise floor. The dotted line is the rms noise for the pupils with a 10 per cent shift (i.e. 90 per cent overlap). In this case low altitude layers have the sensitivity of the overlapping case and for higher layers the sensitivity converges to that of the fully separated case. The initial drop in the curves is due to the strong altitude dependence of the amplitude of the covariance peak, higher layers have larger scintillation signals and so lower noise levels. The increase in noise at higher altitudes is due to the reduction in overlap of the projected pupils, increasing the statistical noise.

This is due to the increase in contrast in the analysis plane image and hence the covariance function.

For partially separated pupils, the amplitude of the covariance peak for a particular layer depends on the separation of the pupils in the analysis plane, $h_{\rm conj}\theta$, and the position of the peak in the autocovariance, $h\theta$. Avila & Cuevas (2009) show exact expressions and approximations for the relative reduction of the covariance peaks, $\epsilon(h\theta)$.

The relative amplitude of the lateral covariance peak is given by $A_2(h\theta) = A_2(1 + \epsilon(h\theta))$ and the central peak is $A_1(h\theta) = A_1(1 + \epsilon(h\theta)/3)$. For overlapping pupils, the coefficients $A_1(h\theta)$ and $A_2(h\theta)$ collapse to A_1 and A_2, respectively, and are as shown in equations (10) and (11). For separated pupils they both converge to unity.

To calculate the sensitivity of generalized-SCIDAR with partially separated pupils we can replace A_1 and A_2 in equation (15) with $A_1(h\theta)$ and $A_2(h\theta)$.

In a standard generalized-SCIDAR set-up, we would expect to conjugate the analysis plane to approximately 2 km below the ground, this generally results in a shift of ∼10 per cent of the telescope diameter in the position of the two lateral set of peaks, $h_{\rm conj}.\theta$. The sensitivity is then altitude dependent with high layers having different $A_1(h\theta)$ and $A_2(h\theta)$ coefficients to the lower layers. The actual values can be calculated using the equations found within Avila & Cuevas (2009). Fig. 7 shows the sensitivity as a function of layer altitude for the three cases of completely overlapping, completely separated and 90 per cent overlapping pupil images in the analysis plane. For this example, $D = 1$ m, $H_0 = 17$ km, $C_n^2 = 100^{-15}$ m$^{-2/3}$ and the target stars are assumed to be the same magnitude.

Although LOLAS also separates the pupil images of the target stars, stereo-SCIDAR still has an advantage when it comes to observing targets with a larger difference in brightness. Having two cameras permits the electron multiplication (EM) gain to be

individually set for each camera, allowing for optimum gain for both targets regardless of stellar magnitude. This allows us to maximize the dynamic range for each pupil image without saturation.

2.4.4 Wind velocity estimation

The wind velocity (speed and direction) of the strongest turbulent layers can be estimated by measuring the movement of the correlation peak of each layer in the spatiotemporal covariance function. If we assume 'frozen' flow of the turbulence, then the scintillation pattern will cross the telescope pupil with the same velocity as the layer. By comparing subsequent frames of the spatiotemporal covariance function the covariance peak will also move allowing estimation of the wind velocity.

Wind velocity profiling is difficult with single camera SCIDAR. This is because each layer contributes three peaks to the covariance function which quickly become spatially confused in the spatiotemporal covariance function. This prohibits the use of geometric algorithms and instead one must identify the layers using a spatiotemporal Fourier analysis. The wavelets approach of García-Lorenzo & Fuensalida (2006) relies on measuring the spatial frequencies inherent in the separation of the correlation peaks. Prieur et al. (2004) developed an automatic algorithm based on a modified CLEAN method. Both procedures require fine parameter tuning and are computationally intensive making an automatic algorithm difficult.

For stereo-SCIDAR we use a geometric algorithm to trace the peaks and calculate vectors between temporally adjacent frames. This is possible due to the lower noise in the covariance function and the fact that we only have one covariance peak per turbulent layer, reducing the possibility of confusion. We calculate the spatiotemporal covariance functions with temporal delays, δt, from -3 frames up to $+3$ frames and the peaks are identified using a Laplacian of Gaussian filter. This involves smoothing the covariance function by convolution with a Gaussian kernel and then a Laplacian operator is used to calculate the second-order spatial derivative of the 2D function, effectively selecting regions with high gradients of intensity. We then select covariance peaks by recording the coordinates of the brightest pixel in the covariance and then subtracting the scaled Gaussian kernel and repeating until there are no peaks above three times the standard deviation of the covariance. This has been automated and we calculate the wind profile along with the turbulence profile for all of our data in real-time. Using the Andor Luca Electron Multiplying Charge Coupled Device (EMCCD) cameras with windowing we attain a frame rate of approximately 90 Hz. For the instrument installed on the 1-m JKT we have 80 pixels across the pupil and we can therefore achieve a wind speed scale of $\sim 1\,\mathrm{m\,s^{-1}\,pixel^{-1}}$. However, this accuracy can be improved by centroiding the correlation peaks to subpixel accuracy. In order to calculate the wind velocity of a layer the covariance peak for that layer must appear in three consecutive frames of the spatiotemporal cross-covariance. Therefore, the maximum wind velocity that can be measured with the 1-m JKT is $36\,\mathrm{m\,s^{-1}}$ and with the 2.5-m NOT is $90\,\mathrm{m\,s^{-1}}$. The worst case is a high layer where the wind direction is such that it is travelling at an angle perpendicular to the line joining the two stars. In this case we would see the layer in the $\mathrm{d}t = 0$ frame but it is possible that it will not appear in any other frame. Therefore, it is possible that high layers will exist for which we cannot obtain velocity estimates. This can be improved by using larger telescopes or narrower targets, increasing the maximum profiling altitude. These high layers will be seen in the spatiotemporal autocovariance and so wind velocities can still be deduced although the altitude information would then be lost.

It is possible to use the wind profile to further enhance the resolution of the optical turbulence profile. Two layers that are unresolved in the turbulence profile may separate in the spatiotemporal cross-covariance due to a difference in wind velocities. Egner & Masciadri (2007) show that this method can be very effective.

3 DATA REDUCTION

In existing SCIDAR systems the intensity patterns from each target overlap on a single detector and the profile is retrieved from the autocovariance function of the combined image. As each pupil image is recorded separately for stereo-SCIDAR the images can be normalized in a way which is not possible with conventional SCIDAR. The images are independently background subtracted, offset to zero mean and scaled to have unit integrated covariance strength. This ensures that despite differing magnitudes of the stars, one does not dominate the other in the cross-covariance. Unlike single-camera generalized-SCIDAR (using the image autocovariance), in stereo-SCIDAR each layer only contributes one peak in the cross-covariance. To retrieve the turbulence profile we are required to solve the inverse problem, written in matrix form

$$B_{**}(\boldsymbol{r}, z) = K_z(\boldsymbol{r}, h)\, C_n^2(h) + n(\boldsymbol{r}), \tag{16}$$

where $B_{**}(\boldsymbol{r}, z)$ is the measured scintillation cross-covariance, $K_z(\boldsymbol{r}, h)$ is the matrix of stereo-SCIDAR responses to unit turbulence at different heights for a given conjugate altitude z and $n(\boldsymbol{r})$ is the noise in the cross-covariance. The inverse problem is solved using a non-negative least-squares inversion (Lawson & Hanson 1974) to retrieve an estimate for the $C_n^2(h)$ profile. A cut of the cross-covariance function from the centre in the direction joining the two target stars is used as the input.

The value of the wavelength used for simulation and data reduction is $\lambda = 500$ nm, which corresponds approximately to the peak of the spectral sensitivity of the detector.

4 RESULTS

Stereo-SCIDAR was operated on the JKT and NOT for a total of 25 nights between 2013 February and September. The results from these observations will be analysed and presented in a future publication. Here we present a selection of interesting examples collected using this system.

4.1 Example profile

Fig. 8 shows the turbulence profile from the JKT, recorded on the night of 2013 September 15 and 16. The analysis plane was set to 0 m to remove any contribution from the dome and ground and hence increase the signal-to-noise ratio of the higher layers. Two targets were observed during the night, the first had a stellar magnitude difference of $\Delta m = 0.7$, the second $\Delta m = 2.7$, both had an angular separation of ~ 10 arcsec. The upper plot shows only the optical turbulence profile. The wind profiles are overlaid on a separate plot for clarity. We do not analyse the profiles in any way here but simply point out a few interesting features that we have seen in the data collected to date. Qualitatively, we see several branching points where a turbulent layer seems to split into two layers and diverge in altitude. We also see the temporal evolution of these turbulent layers, which often seem to be correlated in altitude. The line delineating the maximum altitude is an artefact in the cross-covariance function.
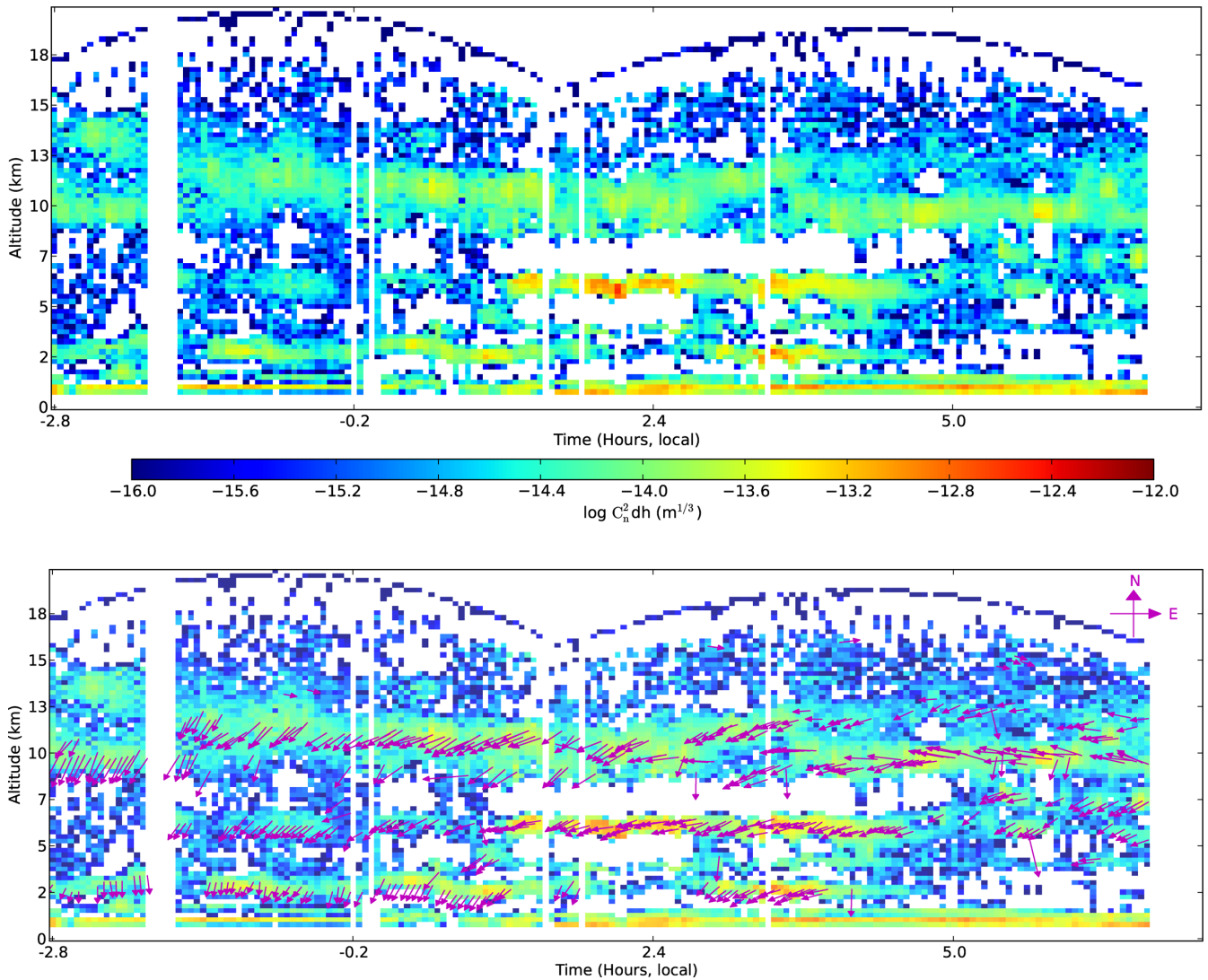
Figure 8. Example turbulence profile from the JKT, La Palma, 2013 September 15. The upper plot shows the profile of the optical turbulence as a function of time. The lower plot is the same but with the layer wind velocities overlaid. The length of the arrows denote the relative wind speed and the direction corresponds to the turbulent layer direction as defined by the cardinal directions shown in the top right of the lower plot. The conjugate altitude of the analysis plane was set to 0 m.

4.2 Wind velocity profiling

Fig. 9 shows the spatiotemporal cross-covariance functions for delays in the range −2 frames up to +2 frames.

If we add the central three frames together (panels b, c and d from Fig. 9), then it becomes easier to see the velocity of each layer (Fig. 10). To build a wind profile we assume frozen flow and implement a geometric algorithm. We make a least-squares fit between equispaced peaks in adjacent frames. We then do the same for several sets of three frames (positive and negative temporal offsets) so that we can detect layers even if they leave the scope of
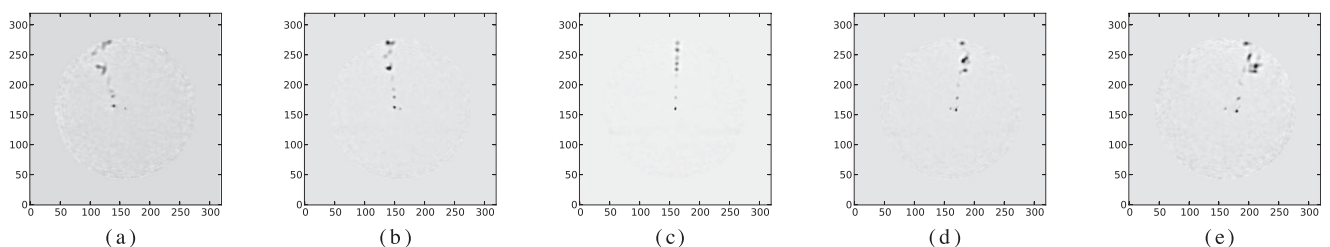
Figure 9. Spatiotemporal cross-covariance functions for the data taken at a conjugate altitude of −2 km (intensity scale inverted for clarity). The plots show cross-covariance functions generated with temporal delays equal to 1 frame (∼10 ms) from −2 frames (a) to +2 frames (e). The case of no temporal delay is shown in (c). By examining the position of these peaks in subsequent frames the wind velocity (magnitude and direction) can be calculated.
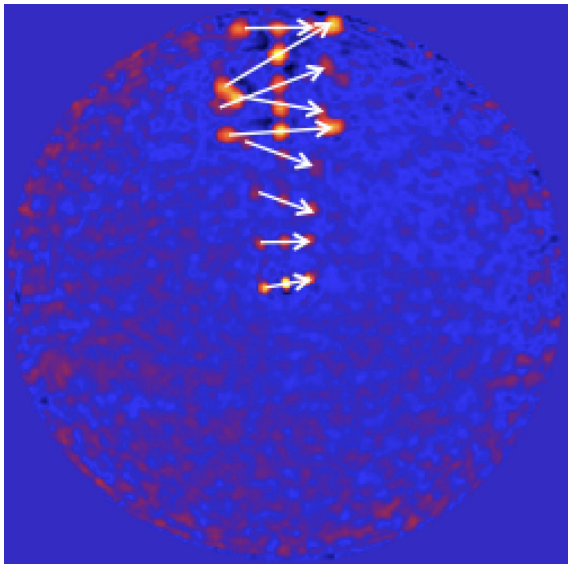
Figure 10. The sum of three consecutive spatiotemporal cross-covariance frames. We show the sum on one image to demonstrate the wind velocity estimation process. The arrows indicate the detected layers and velocities.
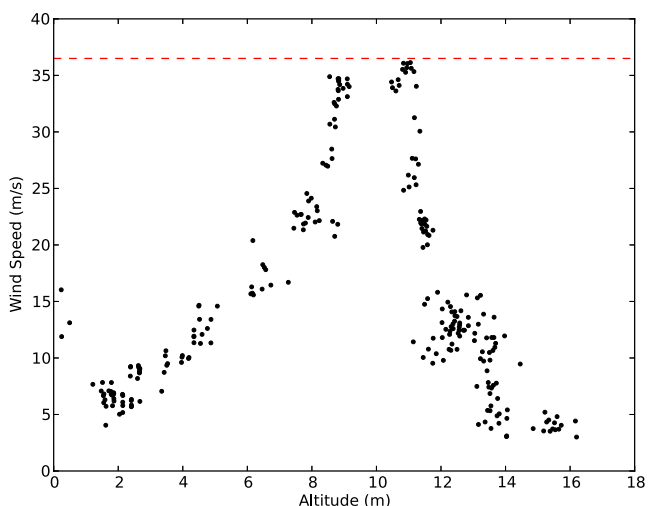

Figure 11. Example distribution of wind speeds as a function of altitude for the night of 2013 September 13, JKT, La Palma. The dashed line indicates the maximum wind speed that can be measured with the current instrument on the JKT. The tropopause can clearly be identified at an altitude of ~10 km.

the cross-covariance function. To detect the velocity of a layer we require it to be seen in at least one set of three frames.

Fig. 11 shows an example distribution of wind speeds as a function of altitude for 160 profiles taken throughout the night of 2013 September 13 from the JKT, La Palma. The dashed line indicates the maximum wind speed that can be measured with the current instrument on the 1-m JKT, with a frame rate of ~72 Hz, this is 36 m s^{-1} (Section 2.4.4).

4.3 Dome seeing estimates

We are able to estimate and remove the contribution of the dome seeing from the covariance function using an extension of the method explained in Avila, Vernin & Cuevas (1998). For dome seeing estimates the conjugate altitude of the analysis plane must be a few

kilometres away from the telescope pupil. Any turbulent layer in the atmosphere will be blown across the pupil of the telescope with some wind speed. Dome seeing will develop slowly and will therefore remain as a peak in the spatiotemporal covariance even with several frames temporal offset. The amplitude of this central peak will slowly decay as the dome seeing decorrelates.

By looking at the amplitude of this central peak as a function of time we will see that only the first few frames will also include the contribution from the surface turbulent layer which will move away from the central position with the velocity of the wind. We can then extrapolate back to zero offset covariance and estimate a value for the covariance value of the dome seeing. Using this technique we are able to remove the dome seeing contribution from the surface turbulent layer strength.

Here we use the spatiotemporal autocovariance function (the covariance of each pupil image with itself). In the autocovariance function any altitude information is removed and all layers appear as covariance peaks at the centre of the covariance function. They then move radially away from the central point in the spatiotemporal autocovariance, with a velocity determined by the velocity of the turbulent layer. The autocovariance is more useful than the cross-covariance for this analysis, as in the spatiotemporal cross-covariance high-altitude layers can move through the central peak, adding noise to the dome seeing estimate. As we are only using the autocovariance this method could be utilized while observing a single star and thus increase the number of targets available. This would also allow us to use a smaller telescope dedicated for dome seeing measurements. Fig. 12 shows measurements of the dome seeing at both the JKT and NOT telescopes.
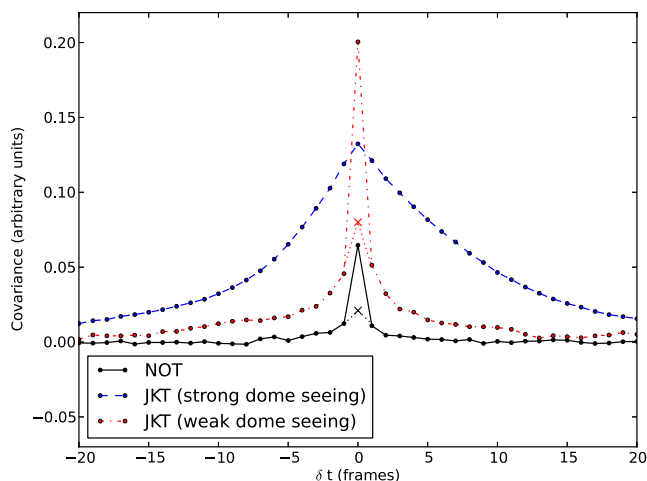

Figure 12. The central value of the autocovariance as a function of temporal delay between the two images. The central spike visible in two of the three curves corresponds to the strength of the external surface layer turbulence. This moves away from the centre of the autocovariance with a velocity given by the wind velocity. The remnant covariance that lingers in the central peak is due to the seeing in the dome of the telescope and decorrelates slowly. The solid curve is for the NOT, anecdotally known for its low dome seeing. We see here that the remnant is extremely small. The dash–dot JKT curve was observed at a time when we did not experience much dome seeing, we do however observe a strong surface layer. By extrapolating the decay of the remnant covariance back to the centre we can estimate the covariance due to the dome seeing (marked by a dotted line and a cross). The dashed curve demonstrates a scenario when we observed very little external turbulence and very strong dome seeing. This was at a time when that outside wind speed was effectively zero and shows that the SCIDAR, as with many remote sensing instruments, fails in these conditions.

5 CONCLUSION

We have developed and tested a new generalized-SCIDAR remote sensing instrument for the characterization of optical turbulence above astronomical sites. In this technique, which we refer to as stereo-SCIDAR, the light from each component of a target double star is imaged on a separate detector. Separating the light from each star allows us to avoid the normalization issue of generalized-SCIDAR, and increases the useable magnitude difference of the targets, resulting in 100 per cent time coverage for La Palma on a 1-m telescope. It also achieves an increase in the signal-to-noise ratio of a factor of 2 for a target pair of stars of the same magnitude, a factor of 3 for $\Delta m = 1$ and a factor of 6.3 if there is 2 mag difference in the brightness of the targets. We have successfully used stereo-SCIDAR with 2.7 mag difference in the target brightness. This yields an increase of a factor of 12 in the sensitivity over single camera SCIDAR. Stereo-SCIDAR also provides a simple, automatic, technique for the detection of the velocity of the atmospheric turbulent layers and the dome seeing.

A limited on-sky test demonstrated the key concepts of the technique. We show several examples from the on-sky data, including an example turbulence profile complete with wind velocity measurements and estimates of the dome seeing for the NOT and JKT.

REFERENCES

Avila R., Cuevas S., 2009, Opt. Express, 17, 10926
Avila R., Vernin J., Masciadri E., 1997, Appl. Opt., 36, 7898
Avila R., Vernin J., Cuevas S., 1998, PASP, 110, 1106
Avila R., Avilés J. L., Wilson R. W., Chun M., Butterley T., Carrasco E., 2008, MNRAS, 387, 1511
Cortés A., Neichel B., Guesalaga A., Osborn J., Rigaut F., Guzman D., 2012, MNRAS, 427, 2089
Egner S. E., Masciadri E., 2007, PASP, 119, 1441
Folcher J.-P., Carbillet M., 2011, Proc. SPIE, 8172, 81721C
Fuchs A., Tallon M., Vernin J., 1994, Proc. SPIE, 2222, 682
Fuchs A., Tallon M., Vernin J., 1998, PASP, 110, 86
García-Lorenzo B., Fuensalida J. J., 2006, MNRAS, 372, 1483
García-Lorenzo B., Fuensalida J. J., 2011, MNRAS, 416, 2123
Lawson C. L., Hanson R. J., 1974, Solving Least Squares Problems. Prentice-Hall, Englewood Cliffs, NJ
Masciadri E., Lascaux F., 2012, Proc. SPIE, 8447, 84475A
Masciadri E., Stoesz J., Hagelin S., Lascaux F., 2010, MNRAS, 404, 144
Osborn J., Wilson R. W., Dhillon V., Avila R., Love G. D., 2011, MNRAS, 411, 1223
Prieur J. L., Daigne G., Avila R., 2001, A&A, 371, 366
Prieur J. L., Avila R., Daigne G., Vernin J., 2004, PASP, 116, 778
Roddier F., 1981, Progress Opt., 19, 281
Tokovinin A., 1997, Study of the SCIDAR Concept for Adaptive Optics Applications. ESO technical report, ESO document, VLT-TRE-UNI-17416-0003
Tokovinin A., 2003, J. Opt. Soc. Am. A, 20, 686
Tokovinin A., Kornilov V., 2007, MNRAS, 381, 1179
Vernin J., Roddier F., 1973, J. Opt. Soc. Am., 63, 270
Wilson R. W., 2002, MNRAS, 337, 103

This paper has been typeset from a TeX/LaTeX file prepared by the author.